

# Iterative Correction Scheme Based on Discrete Cosine Transform and L1 Regularization for Fluorescence Molecular Tomography With Background Fluorescence

Jiulou Zhang, Junwei Shi, Huizhi Guang, Simin Zuo, Fei Liu, Jing Bai, *Fellow, IEEE*,  
and Jianwen Luo\*, *Senior Member, IEEE*

**Abstract**—**Goal:** High-intensity background fluorescence is generally encountered in fluorescence molecular tomography (FMT), because of the accumulation of fluorescent probes in nontarget tissues or the existence of autofluorescence in biological tissues. The reconstruction results are affected or even distorted by the background fluorescence, especially when the distribution of fluorescent targets is relatively sparse. The purpose of this paper is to reduce the negative effect of background fluorescence on FMT reconstruction. **Methods:** After each iteration of the Tikhonov regularization algorithm, 3-D discrete cosine transform is adopted to filter the intermediate results. And then, a sparsity constraint step based on L1 regularization is applied to restrain the energy of the objective function. **Results:** Phantom experiments with different fluorescence intensities of homogeneous and heterogeneous background are carried out to validate the performance of the proposed scheme. The results show that the reconstruction quality can be improved with the proposed iterative correction scheme. **Conclusion and Significance:** The influence of background fluorescence in FMT can be reduced effectively because of the filtering of the intermediate results, the detail preservation, and noise suppression of L1 regularization.

**Index Terms**—Background fluorescence, discrete cosine transform (DCT), fluorescence molecular tomography (FMT).

## I. INTRODUCTION

AS a promising imaging modality, fluorescence molecular tomography (FMT) is capable of quantitatively detecting and analyzing the 3-D distribution of fluorescent probes in small

animals *in vivo* [1]. However, background fluorescence is generally encountered in the process of FMT reconstruction, which is caused by the autofluorescence of biological tissues or the distribution of fluorescent probes in the nontarget region. The reconstruction quality is greatly decreased for the existence of background fluorescence.

In past years, several methods have been proposed to reduce the influence of background fluorescence. The subtraction of average fluorescence response from raw data was proposed in [2], which was accomplished by cubic polynomial fitting to Born values. Different subtraction methods based on the physical models of photon propagation were proposed in [3]. Anatomical information from X-CT modality was combined with bulk fluorescence detection to increase the detection sensitivity, and data-driven fluorescence background estimator was used for background fluorescence subtraction [4]. These three methods mainly aim at the preprocessing of raw fluorescence data. Besides, the shape-based reconstruction method using spherical harmonic parameterization was developed [5], in which the distribution of fluorescent targets was assumed to be piecewise constant and the remaining region was background. In this reconstruction method, the fluorescent targets and background can be recovered simultaneously, but the solutions are dependent on initial conditions to some extent.

In this paper, an iterative correction scheme based on 3-D discrete cosine transform (DCT) and L1 regularization is employed in each iteration of the Tikhonov regularization algorithm. Unlike the fluorescence data correction methods mentioned above, the proposed scheme does not need the preprocessing of raw fluorescence data. The intermediate results obtained in each iteration of Tikhonov regularization are first filtered by 3-D DCT. Then, a sparsity constraint based on L1 regularization is adopted to restrain the filtered results. The final reconstruction results can be improved significantly because of the filtering of the intermediate results, and the detail preservation and noise suppression of L1 regularization.

The outline of this paper is organized as follows. The proposed method is described in detail in Section II. Section III describes the setup of phantom experiments, materials, reconstruction algorithms, and parameters. Section IV shows the reconstruction results and corresponding quantitative analysis. Finally, the discussion and conclusion are presented in Section V.

Manuscript received May 15, 2015; revised August 10, 2015; accepted September 23, 2015. Date of publication September 29, 2015; date of current version May 18, 2016. This work was supported by the National Basic Research Program of China (973) under Grant 2011CB707701; the National Natural Science Foundation of China under Grant 81227901, Grant 81271617, Grant 61322101, and Grant 61401246; the National Major Scientific Instrument and Equipment Development Project under Grant 2011YQ030114; the National Science and Technology Support Program under Grant 2012BA123B00; and the China Postdoctoral Science Foundation under Grant 2014M550073. Asterisk indicates corresponding author.

J. Zhang, J. Shi, H. Guang, S. Zuo, and J. Bai are with the Department of Biomedical Engineering, School of Medicine, Tsinghua University.

F. Liu is with the Tsinghua-Peking Center for Life Sciences and the Department of Biomedical Engineering, School of Medicine, Tsinghua University.

\*J. Luo is with the Center for Biomedical Imaging Research and the Department of Biomedical Engineering, School of Medicine, Tsinghua University, Beijing 100084, China (e-mail: luo\_jianwen@tsinghua.edu.cn).

Color versions of one or more of the figures in this paper are available online at <http://ieeexplore.ieee.org>.

Digital Object Identifier 10.1109/TBME.2015.2483539

## II. METHODS

### A. Forward Model

The photon propagation in biological tissues is commonly described by the diffusion equation (DE) known as the lower order approximation of radiative transfer equation [6]

$$[-\nabla D \nabla + \mu_a] G(r, r_s) = -\delta(r - r_s) \quad (1)$$

where  $G(r, r_s)$  denotes Green's function of photons propagation from the source position  $r_s$  to an arbitrary position  $r$ , and  $\delta(r - r_s)$  is the excitation source.  $D = 1/3(\mu_a + \mu'_s)$  is the diffusion coefficient of biological tissue, while  $\mu_a$  and  $\mu'_s$  are the absorption coefficient and reduced scattering coefficient, respectively.

After the image domain being discretized into tens of thousands of or even more small cubes, Kirchhoff approximation [7] is used to solve the DE. Then, FMT problem can be linearized as the following weight matrix equation:

$$WX = b \quad (2)$$

where  $W$  is the weight matrix,  $b$  denotes the fluorescence intensity, and  $X$  is the fluorescent targets to be reconstructed.

### B. Tikhonov Regularization Algorithm

The iterated Tikhonov regularization method [8] is generally used to solve (2). The corresponding optimization function can be written as follows:

$$\arg \min_{X \geq 0} \|WX - b\|_2^2 + \lambda \|X\|_2^2 \quad (3)$$

where  $\lambda$  is the regularization parameter. According to the generalized inverse of matrices, (3) can be solved in the right inverse formation when the number of rows of  $W$  is much smaller than the number of columns

$$X_k = X_{k-1} - W'[(WW' + \lambda \times \text{tr}(WW'))^{-1}(WX_{k-1} - b)]. \quad (4)$$

When the number of rows of  $W$  is much larger than the number of columns, (3) can be solved in the left inverse formation

$$X_k = X_{k-1} - (W'W + \lambda \times \text{tr}(W'W))^{-1}[W'(WX_{k-1} - b)]. \quad (5)$$

However, the intermediate results are generally affected or even distorted in each iteration of the Tikhonov regularization algorithm, because the original fluorescence data are contaminated by background fluorescence with high intensity. Thus, the intermediate results need to be further corrected or restrained, like the denoising scheme proposed in [9].

### C. DCT Filter

A large amount of noise would be introduced in the intermediate results after each iteration of the Tikhonov regularization algorithm. However, the noise can be discriminated easier in the transformation domain by discrete Fourier transform, wavelet transform, DCT, etc. [10]–[12]. Since the noise mainly exists in the high frequency of the transformation domain, DCT is adopted in this paper to filter the intermediate results. The

fluorescent targets to be reconstructed are 3-D in space; thus, the DCT coefficient matrix  $F(u, v, w)$  of the image domain  $f(x, y, z)$  can be constructed as follows:

$$F(u, v, w) = \sqrt{\frac{8}{MNL}} g_u g_v g_w \sum_{x=0}^{M-1} \sum_{y=0}^{N-1} \sum_{z=0}^{L-1} f(x, y, z) \cos \frac{(2x+1)u\pi}{2M} \cos \frac{(2y+1)v\pi}{2N} \cos \frac{(2z+1)w\pi}{2L} \quad (6)$$

$$g_u = \begin{cases} \frac{1}{\sqrt{2}}, & u = 0 \\ 1, & u \neq 0 \end{cases}, \quad g_v = \begin{cases} \frac{1}{\sqrt{2}}, & v = 0 \\ 1, & v \neq 0 \end{cases}, \quad g_w = \begin{cases} \frac{1}{\sqrt{2}}, & w = 0 \\ 1, & w \neq 0 \end{cases} \quad (7)$$

where  $M$ ,  $N$ , and  $L$  are numbers of image domain elements in  $x$ ,  $y$ , and  $z$  coordinate directions, respectively. The DCT coefficient matrix  $D$  of vector  $X_k$  is extracted from  $F(u, v, w)$  according to the locations of  $X_k$  elements in the image domain  $f(x, y, z)$ . And then  $X_k^{\text{dct}}$ , which is the DCT of  $X_k$ , can be obtained by

$$X_k^{\text{dct}} = DX_k. \quad (8)$$

Because the noise tends to be concentrated in a few high-frequency components (i.e., the small values of  $X_k^{\text{dct}}$ ), the values in  $X_k^{\text{dct}}$  smaller than a preset threshold  $T \times \max(\text{abs}(X_k^{\text{dct}}))$  are set to zero. After that, the filtered intermediate result  $X_k^D$  can be calculated from  $X_k^{\text{dct}}$  left multiplied by the inverse of  $D$ , as

$$X_k^D = D^{-1} X_k^{\text{dct}}. \quad (9)$$

### D. Sparsity Constraint Based on L1 Regularization

The distribution of fluorescent targets to be reconstructed is generally sparse; thus, the constraint based on L1 regularization is applied in this paper

$$\arg \min_{\hat{X}_k^D \geq 0} \|H \hat{X}_k^D - X_k^D\|_2^2 + \tau \|\hat{X}_k^D\|_1 \quad (10)$$

where  $H$  is an observation matrix,  $\tau = \Psi \times \max(\text{abs}(H' X_k^D))$  is the regularization parameter, and  $\hat{X}_k^D$  is the corrected column vector based on L1 regularization. An identity matrix is considered as the observation matrix  $H$  in this paper. The iterative shrinkage/thresholding (IST) algorithms have been demonstrated to be capable of handling the convex optimization problem like image restoration effectively [13], [14]. Removing the negative effect of background fluorescence in FMT is also considered as image restoration to some extent. Thus, the two-step IST algorithm (TwIST) [15] is adopted to solve (10) in this paper.

The iterative correction scheme based on DCT and L1 regularization can be summarized as follows.

- 1) The intermediate result  $X_k$  of (3) is computed from the Tikhonov algorithm, and the negative values in  $X_k$  are set to zero.

- 2) The 3-D DCT coefficient matrix  $D$  is constructed according to the locations of  $X_k$  elements in the image domain  $f(x, y, z)$ .
- 3)  $X_k^{\text{dct}}$  is obtained by calculating  $DX_k$ , and then, the values in  $X_k^{\text{dct}}$  smaller than the preset threshold  $T \times \max(\text{abs}(X_k^{\text{dct}}))$  are set to zero.
- 4) The filtered result  $X_k^D$  can be obtained by computing  $D^{-1}X_k^{\text{dct}}$ .
- 5) The corrected result vector  $\hat{X}_k^D$  is obtained by solving (10) with the TwIST algorithm, and then, the negative values in  $\hat{X}_k^D$  are set to zero.
- 6)  $k = k + 1$ , and go to step 1 until  $k > K$ .

### III. PHANTOM EXPERIMENTS

#### A. Experimental Setup

The performance of the proposed scheme was tested in phantom experiments with homogeneous and heterogeneous background, respectively. Phantom experiments were conducted on a stand-alone noncontact full-angle FMT system previously developed in our laboratory [16]. In the experiments, the point excitation source was provided by a 250-W Halogen lamp (7ILT250, 7-star, Beijing, China). A  $775 \pm 23$  nm bandpass filter (FF01-775/46-25, Semrock, Rochester, NY, USA) was employed in front of the Halogen lamp as the excitation filter and an  $840 \pm 6$  nm bandpass filter (FF01-840/12-25, Semrock, Rochester, NY, USA) was used in front of the charge-coupled device camera for fluorescence data collection.

#### B. Materials

A transparent glass cylinder (5.5-cm height and 2.8-cm diameter) filled with a mixture of 1% intralipid, indocyanine green (ICG) and deionized water ( $\mu_a = 0.02 \text{ cm}^{-1}$  and  $\mu'_s = 10 \text{ cm}^{-1}$ ) was used as the phantom. Three kinds of phantom experiments were performed, i.e., the experiment with homogeneous background (Experiment 1), the experiment heterogeneous background and same strength of fluorescent targets (Experiment 2), and the experiment with heterogeneous background and different strengths of fluorescent targets (Experiment 3).

In Experiment 1, the concentration of background fluorophores (i.e., ICG) was  $2.0 \mu\text{M}$ . Two small transparent glass tubes with a diameter of 0.4 cm filled with  $30 \mu\text{L}$  ICG ( $10 \mu\text{M}$  in concentration) were immersed in the phantom as the fluorescent targets with an edge-to-edge distance of 0.6 cm [one located at  $(0, -0.5, 2.7 \text{ cm})$ , the other located at  $(0, 0.5, 2.7 \text{ cm})$ ]. Thus, the concentration ratio of the background fluorophore and fluorescent targets was 1 : 5. Besides, two glass tubes (0.4 cm in diameter) filled with 1% intralipid, ink, and deionized water were embedded into the phantom as the absorptive rods ( $\mu_a = 1.0 \text{ cm}^{-1}$ ,  $\mu'_s = 10 \text{ cm}^{-1}$ ). The edge-to-edge distance of the two absorptive rods was 0.15 cm [one located at  $(-0.275, 0, 2.7 \text{ cm})$ , the other located at  $(0.275, 0, 2.7 \text{ cm})$ ]. The front and transverse views of this phantom setting are shown in Fig. 1(a) and (b), respectively.

In Experiment 2, three different concentrations of fluorophores (3, 2, and  $1 \mu\text{M}$ , respectively) were combined together

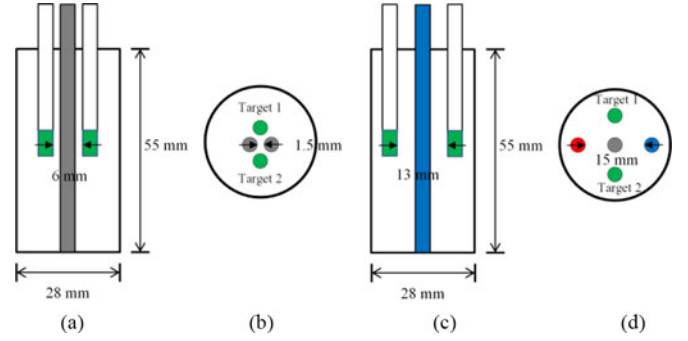


Fig. 1. Setup of phantom experiments. (a) Front view and (b) transverse view of the phantom with homogeneous background. Green regions are the double fluorescent targets, gray regions denote the absorber rods, and blank region is the fluorescence background. (c) Front view and (d) transverse view of phantom with heterogeneous background. Green regions are the double fluorescent targets; gray regions denote the absorber rod. Red, blue, and blank regions are the fluorescence background with different concentrations of ICG, respectively.

as the heterogeneous background. The concentration of background fluorophore (ICG) in the phantom was  $3 \mu\text{M}$ . Two glass tubes with a diameter of 0.4 cm filled with a mixture of 1% intralipid, ICG (2 and  $1 \mu\text{M}$ , respectively) and deionized water were embedded into the phantom with an edge-to-edge distance of 1.5 cm. As shown in Fig. 1(d), the red region denotes the background fluorophore with a concentration of  $1 \mu\text{M}$  [located at  $(-0.95, 0, 3.2 \text{ cm})$ ], while the blue region was the background fluorophore with a concentration of  $2 \mu\text{M}$  [located at  $(0.95, 0, 3.2 \text{ cm})$ ]. Furthermore, one glass tube (diameter 0.4 cm) filled with 1% intralipid, ink, and deionized water was embedded into the phantom as the absorptive rod ( $\mu_a = 0.5 \text{ cm}^{-1}$ ,  $\mu'_s = 10 \text{ cm}^{-1}$ ), which was located at the center of phantom. Two small transparent glass tubes with a diameter of 0.4 cm filled with  $30 \mu\text{L}$  ICG ( $10 \mu\text{M}$  in concentration) were embedded into the phantom as the fluorescent targets. The edge-to-edge distance of them was 1.3 cm [one located at  $(0, 0.85, 3.2 \text{ cm})$ , the other at  $(0, -0.85, 3.2 \text{ cm})$ ].

In Experiment 3, the absorption coefficient  $\mu_a$  of heterogeneous background shown in the red and green regions of Fig. 1(c) and (d) was set to  $0.1 \text{ cm}^{-1}$ , and the concentrations of two fluorescent targets were  $10 \mu\text{M}$  (Target 1) and  $13 \mu\text{M}$  (Target 2), respectively. The rest of setup in this experiment was kept the same as the previous ones.

In this paper, 36 fluorescence projections were collected in  $10^\circ$  steps and the field of view of detection was approximately  $90^\circ$ .

#### C. Reconstruction Algorithms

In order to validate the performance of the proposed scheme, two commonly used reconstruction algorithms, i.e., Tikhonov regularization [17] and restarted L1-regularized nonlinear conjugate gradient (re-L1-NCG) [18], were both employed for comparison in this paper. Both algorithms had been demonstrated to achieve good performance in FMT reconstruction without background fluorescence. The regularization parameter  $\lambda$  and the iterations  $K$  for solving (3) were empirically set to  $1 \times 10^{-4}$  and 70 for the phantom experiment with homogeneous



background,  $1 \times 10^{-5}$  and 20 for the two phantom experiments with heterogeneous background, respectively. For the three cases,  $T$  was set to 0.015 in the filter of 3-D DCT, and  $\Psi$  was set to 0.1 for solving (10). The reconstruction was implemented on a personal computer with Intel Core™ i7-2600 CPU @ 3.40 GHz and 8.00-GB RAM.

#### D. Evaluation Metrics

In order to analyze the reconstruction results, the normalized intensity profile, average value (AVG), relative error (RE), and contrast-to-noise ratio (CNR) are adopted as the evaluation indexes in this paper. The normalized intensity profile obtained across the fluorescent targets in the reconstructed slice image is used to measure the spatial resolution. The AVG, calculated as the average value of fluorescence yields within the 3-D volume of interest (VOI) where each fluorescent target is located, is used to reflect the absolute quantitative results of different fluorescent targets. The RE represents the relative error between the normalized reconstructed slice image and the true one and is defined as follows:

$$RE = \|X_{\text{rec}} - X_{\text{true}}\|^2 / \|X_{\text{true}}\|^2 \quad (11)$$

where  $X_{\text{rec}}$  is the reconstructed slice results and  $X_{\text{true}}$  denotes true slice data excluding the background. The CNR describes whether the fluorescent targets are well recovered in the target region or lost in background and is defined as

$$CNR = \frac{\mu_{\text{VOI}} - \mu_{\text{BCK}}}{(w_{\text{VOI}}\sigma_{\text{VOI}}^2 + w_{\text{BCK}}\sigma_{\text{BCK}}^2)^{1/2}} \quad (12)$$

where  $\mu_{\text{VOI}}$  is the mean value of fluorescence yields within the VOI where the fluorescent targets are located; and  $\mu_{\text{BCK}}$  is the mean value of fluorescence yields over the 3-D region of background (BCK).  $w_{\text{VOI}} = A_{\text{VOI}}/(A_{\text{VOI}} + A_{\text{BCK}})$  and  $w_{\text{BCK}} = A_{\text{BCK}}/(A_{\text{VOI}} + A_{\text{BCK}})$  are the weights of the VOI and BCK, where  $A_{\text{VOI}}$  and  $A_{\text{BCK}}$  are the areas of the VOI and BCK, respectively.  $\sigma_{\text{VOI}}^2$  and  $\sigma_{\text{BCK}}^2$  are the variances of fluorescence yields in the VOI and BCK, respectively.

### IV. RESULTS

#### A. Phantom Results With Homogeneous Background

The slice and 3-D view of the true double fluorescent targets are shown in Fig. 2(a) and (f). And the reconstruction results obtained from the Tikhonov and re-L1-NCG algorithms are shown in Fig. 2(b), (g) and Fig. 2(c), (h), respectively. It can be seen that the results are distorted seriously because the fluorescence data used for reconstruction are contaminated with the high-intensity background fluorescence in the phantom. Fig. 2(d) and (i) shows that the slice and 3-D view of the results obtained from the proposed ICS method but without DCT (ICS). As can be seen, the reconstruction quality is improved significantly on account of the sparsity correction based on L1 regularization in each iteration of the Tikhonov algorithm. More importantly, the reconstruction results obtained from ICS with 3-D DCT (ICS-DCT) shown in Fig. 2(e) and (j) have been further improved compared with the results obtained from ICS [see Fig. 2(d) and (i)].

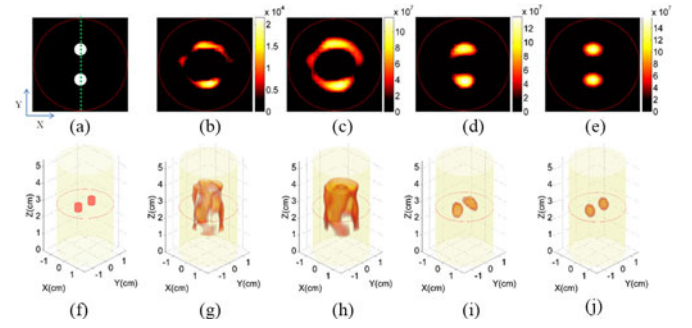


Fig. 2. Reconstruction results of the phantom experiment with homogeneous background using different methods. (a), (f) Slice and 3-D view of the true double fluorescent targets. (b), (g) Slice and 3-D view of the reconstructed images obtained from the re-L1-NCG method. (c), (h) Slice and 3-D view of the reconstructed images obtained from Tikhonov regularization. (d), (e), (i), (j) Slice and 3-D view of reconstructed images obtained from ICS and ICS-DCT, respectively.

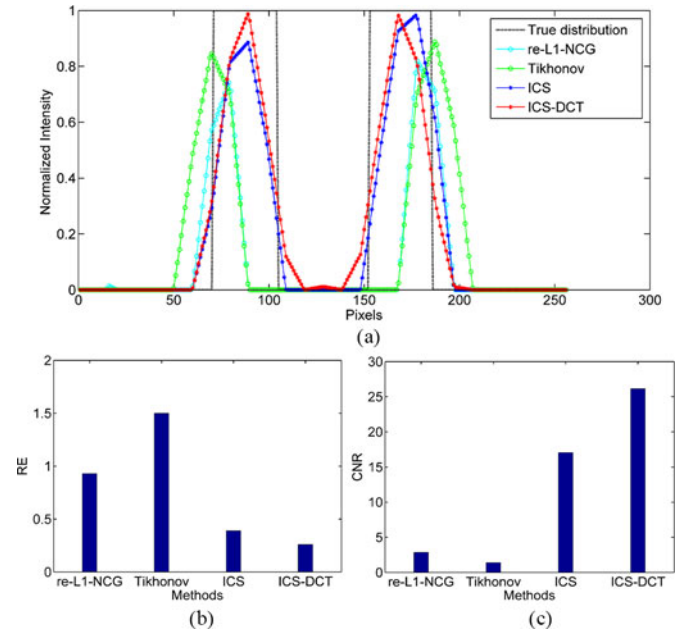


Fig. 3. Relative quantitation analysis of the reconstruction results in Fig. 2. (a) Normalized intensity profiles along the dotted line in Fig. 2(a) using different methods. (b) REs of the slice results in Fig. 2(b)–(e) obtained from different methods. (c) CNRs of the 3-D results in Fig. 2(g)–(j) using different methods.

The normalized intensity profiles along the dotted line in Fig. 2(a), REs, and CNRs are shown in Fig. 3. As can be seen from Fig. 3(a), the intensity profiles obtained from ICS and ICS-DCT match better with the true profile than those obtained from the re-L1-NCG and Tikhonov algorithms. The REs in Fig. 3(b) show the performance of different methods more clearly. The REs of the reconstruction results obtained from the re-L1-NCG and Tikhonov algorithms are significantly higher than those of the proposed scheme because of the distortion of the reconstruction results. Furthermore, the RE of the results obtained from ICS-DCT is slightly lower than that of the results obtained from ICS, because the intermediate results are filtered by 3-D DCT before the sparsity correction based on L1 regularization. As shown in Fig. 3(c), the CNR of the results obtained from ICS-DCT is higher than that from ICS.

TABLE I  
AVGS OF DIFFERENT FLUORESCENT TARGETS WITHIN THE CORRESPONDING  
VOIS OBTAINED FROM DIFFERENT METHODS

Experiments	Fluorescent Targets	Methods			
		re-L1-NCG	Tikhonov	ICS	ICS-DCT
Experiment 1	Target 1	$3.74 \times 10^3$	$2.83 \times 10^7$	$8.56 \times 10^7$	$9.76 \times 10^7$
	Target 2	$4.22 \times 10^3$	$2.77 \times 10^7$	$8.90 \times 10^7$	$9.77 \times 10^7$
	Ratio	0.88:1	1.02:1	0.96:1	1.00:1
Experiment 2	Target 1	$2.60 \times 10^3$	$1.21 \times 10^9$	$8.89 \times 10^8$	$7.82 \times 10^8$
	Target 2	$3.00 \times 10^3$	$1.00 \times 10^9$	$7.14 \times 10^8$	$7.51 \times 10^8$
	Ratio	0.87:1	1.21:1	1.25:1	1.04:1
Experiment 3	Target 1	$3.21 \times 10^3$	$7.89 \times 10^8$	$5.07 \times 10^8$	$6.00 \times 10^8$
	Target 2	$3.41 \times 10^3$	$9.51 \times 10^8$	$6.87 \times 10^8$	$6.70 \times 10^8$
	Ratio	0.94:1	0.83:1	0.74:1	0.89:1

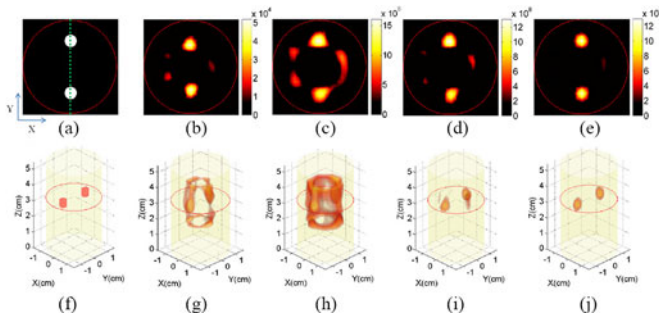


Fig. 4. Reconstruction results of the phantom experiment with heterogeneous background and same strength of fluorescent targets. (a), (f) Slice and 3-D view of the true double fluorescent targets. (b), (g) Slice and 3-D view of the reconstructed images obtained from the re-L1-NCG method. (c), (h) Slice and 3-D view of the reconstructed images obtained from Tikhonov regularization. (d), (e), (i), (j) Slice and 3-D view of reconstructed images obtained from ICS and ICS-DCT, respectively.

In Experiment 1, the AVGs obtained from different methods are listed in Table I. The AVGs obtained from the proposed ICS-DCT method are higher than those from Tikhonov and ICS, but the ratio of AVGs of two fluorescent targets obtained from ICS-DCT is still recovered well.

### B. Phantom Results With Heterogeneous Background

Fig. 4 shows the reconstruction results of the phantom experiment with heterogeneous background and same strength of two fluorescent targets. Fig. 4(a) and (f) shows the slice and 3-D view of the true double fluorescent targets. Fig. 4(b), (g) and Fig. 4(c), (h) compare the reconstruction results obtained from the Tikhonov and re-L1-NCG methods, respectively. Although their slice results are not distorted seriously compared with the results in Fig. 2(b) and (c), some useless information is still distributed in the 3-D reconstruction results extensively [see Fig. 4(g) and (h)]. Fig. 4(d) and (i) shows the slice and 3-D view of the results obtained ICS. The reconstruction quality is improved significantly on account of the sparsity correction based on L1 regularization in each iteration of the Tikhonov algorithm. In addition, the reconstruction results obtained from ICS-DCT [see Fig. 4(e) and (j)] have been further improved by the DCT filter compared with the results obtained from ICS [see Fig. 4(d) and (i)].

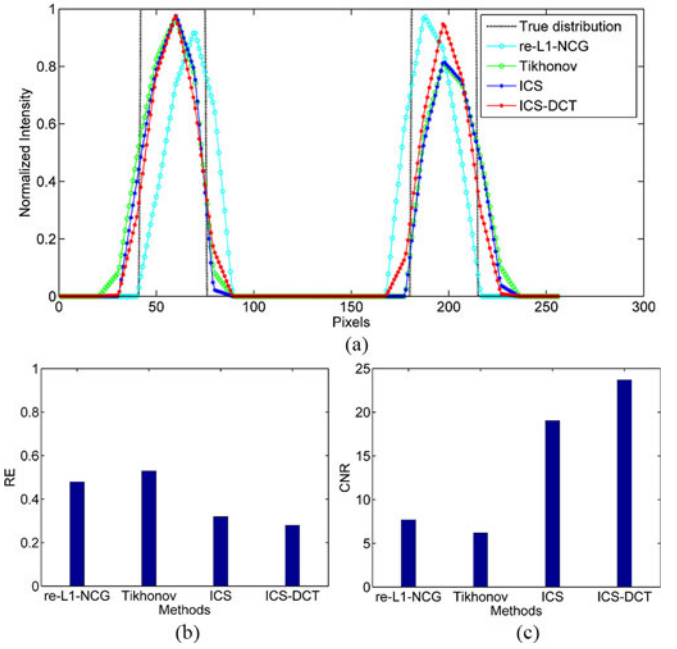


Fig. 5. Relative quantitation analysis of the reconstruction results in Fig. 4. (a) Normalized intensity profiles along the dotted line in Fig. 4(a) using different methods. (b) REs of the slice results in Fig. 4(b)–(e) obtained from different methods. (c) CNRs of the 3-D results in Fig. 4(g)–(j) using different methods.

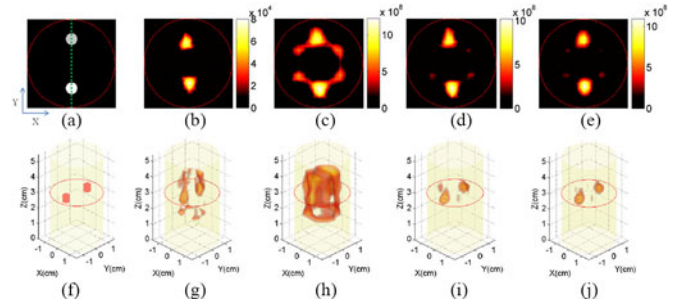


Fig. 6. Reconstruction results of the phantom experiment with heterogeneous background and different strengths of fluorescent targets. (a), (f) Slice and 3-D view of the true double fluorescent targets. (b), (g) Slice and 3-D view of the reconstructed images obtained from the re-L1-NCG method. (c), (h) Slice and 3-D view of the reconstructed images obtained from Tikhonov regularization. (d), (e), (i), (j) Slice and 3-D view of reconstructed images obtained from ICS and ICS-DCT, respectively.

The relative quantitation analysis of the reconstruction results is shown in Fig. 5. It can be seen in Fig. 5(a) that the location of the fluorescent targets is similar in all profiles except the profile of the results obtained from re-L1-NCG. The REs in Fig. 5(b) show that the error of the slice result in Fig. 4(e) is the lowest in all reconstruction results. The CNRs of the 3-D results [see Fig. 4(g)–(j)] are shown in Fig. 5(c), which illustrates that the CNRs of the results obtained from Tikhonov and re-L1-NCG are significantly lower than that of the results from the proposed scheme. In addition, the CNR of the results from ICS-DCT is again higher than that of ICS.

The AVGs of the reconstructed results for Experiment 2 are listed in Table I. The AVGs obtained from the proposed ICS-DCT method are lower than those from Tikhonov. And the ratio

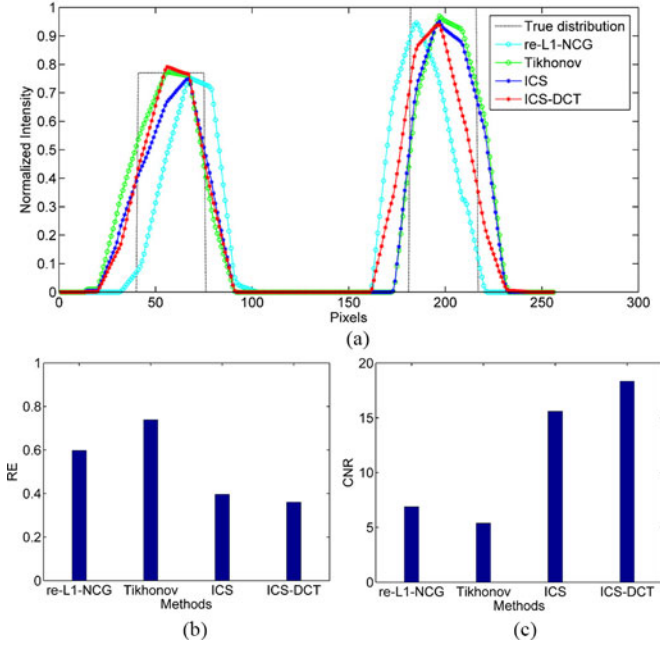


Fig. 7. Relative quantitation analysis of the reconstruction results in Fig. 6. (a) Normalized intensity profiles along the dotted line in Fig. 6(a) using different methods. (b) REs of the slice results in Fig. 6(b)–(e) obtained from different methods. (c) CNRs of the 3-D results in Figs. 6(g)–(j) using different methods.

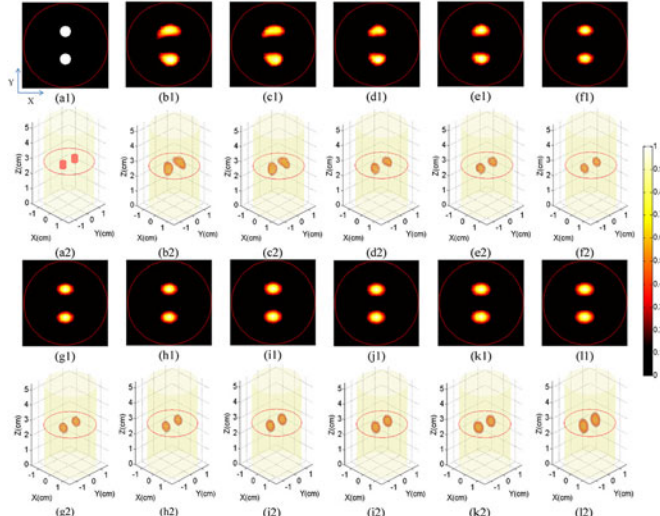


Fig. 8. Influence of different thresholds  $T$  on the reconstruction results of the phantom experiment with homogeneous background. (a1), (a2) Slice and 3-D view of the true double fluorescent targets. (b1), (b2) Slice and 3-D view of reconstructed images obtained from ICS. (c1)–(i1) Slice view of the reconstruction results obtained from ICS-DCT with different  $T$  from 0.002 to 0.02 in 0.002 steps. (c2)–(i2) Three-dimensional view of the reconstruction results obtained from ICS-DCT with different  $T$  from 0.002 to 0.02 in 0.002 steps. All images are normalized by the maximal values of the reconstruction results.

of AVGs of different fluorescent targets obtained from ICS-DCT is better recovered than the other methods.

The reconstruction results of the phantom experiment with heterogeneous background and different strengths of fluorescent targets obtained from different methods are shown in Fig. 6. Fig. 6(a) and (f) shows the slice and 3-D view of the true double fluorescent targets. Fig. 6(b) and (g) shows the slice and

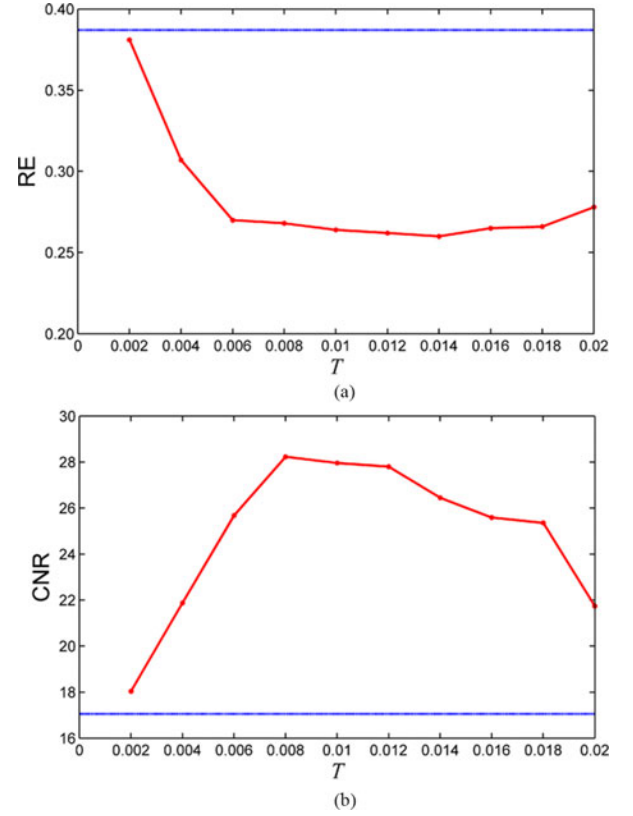


Fig. 9. Relative quantitation analysis of the reconstruction results in Fig. 8. (a) REs of the slice results in Fig. 8(b1)–(i1) obtained from different methods. (b) CNRs of the 3-D results in Fig. 8(b2)–(i2) obtained using different methods. The red line describes the REs and CNRs of the results obtained from ICS-DCT with different  $T$ . The blue line denotes the RE and CNR of the results obtained from ICS.

3-D view of the reconstruction results obtained from re-L1-NCG, in which two reconstructed fluorescent targets are deviated from the true targets [see Fig. 6(a) and (f)]. Fig. 6(c) and (h) shows slice and 3-D view of reconstruction results obtained from Tikhonov. Useless information is still distributed extensively in these results [see Fig. 6(g) and (h)]. Fig. 6(d) and (i) shows the slice and 3-D view of the results obtained ICS, which have been significantly improved compared with the results from re-L1-NCG and Tikhonov [see Fig. 6(b), (g), (c), and (h)]. As can be seen, the reconstruction results obtained from the proposed ICS-DCT method [see Fig. 6(e) and (j)] are closest to the true results [see Fig. 6(a) and (f)].

Fig. 7 shows that the relative quantitation analysis of the reconstruction results. As shown in the normalized intensity profiles [see Fig. 7(a)], the strength ratio of fluorescent targets can be reflected by different methods. But the profile obtained from re-L1-NCG has the worst match with the true distribution profile. Fig. 7(b) and (c) shows the REs and CNRs of the reconstruction results obtained from different methods. The RE and CNR of the results obtained from the proposed ICS-DCT method are the lowest and highest among the three methods, respectively.

In Experiment 3, the AVGs of the reconstructed results are listed in Table I. The AVGs obtained from ICS-DCT are lower



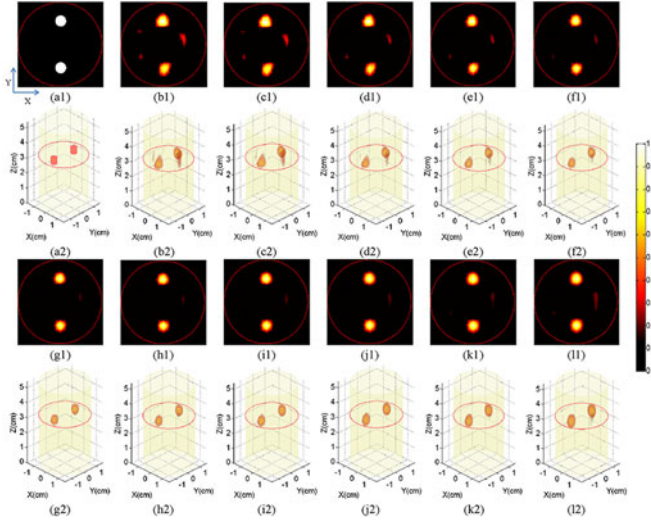


Fig. 10. Influence of different thresholds  $T$  on the reconstruction results of the phantom experiment with heterogeneous background and same strength of fluorescent targets. (a1), (a2) Slice and 3-D view of the true double fluorescent targets. (b1), (b2) Slice and 3-D view of reconstructed images obtained from ICS. (c1)–(f1) Slice view of the reconstruction results obtained from ICS-DCT with different  $T$  from 0.002 to 0.02 in 0.002 steps. (c2)–(f2) Three-dimensional view of the reconstruction results obtained from ICS-DCT with different  $T$  from 0.002 to 0.02 in 0.002 steps. All images are normalized by the maximal values of the reconstruction results.

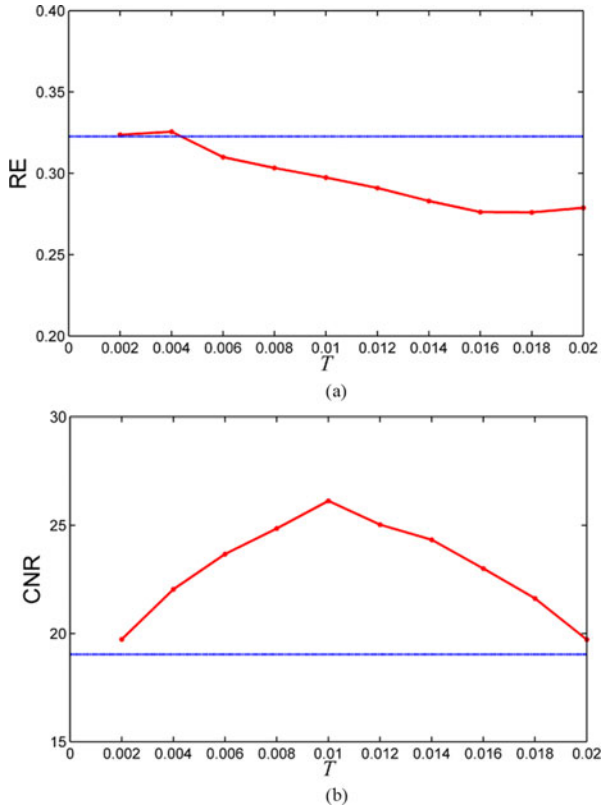


Fig. 11. Relative quantitation analysis of the reconstruction results in Fig. 10. (a) REs of the slice results in Fig. 10(b1)–(f1) obtained from different methods. (b) CNRs of the 3-D results in Fig. 10(b2)–(f2) obtained using different methods. The red line describes the REs and CNRs of the results obtained from ICS-DCT with different  $T$ . The blue line denotes the RE and CNR of the results obtained from ICS.

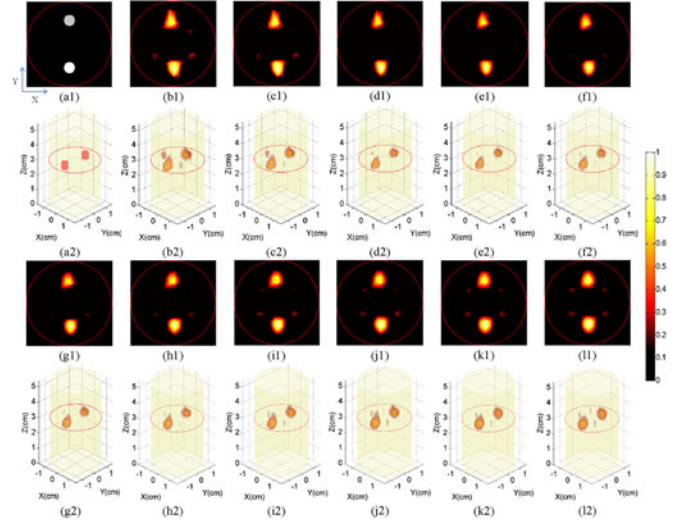


Fig. 12. Influence of different thresholds  $T$  on the reconstruction results of the phantom experiment with heterogeneous background and different strengths of fluorescent targets. (a1), (a2) Slice and 3-D view of the true double fluorescent targets. (b1), (b2) Slice and 3-D view of reconstructed images obtained from ICS. (c1)–(f1) Slice view of the reconstruction results obtained from ICS-DCT with different  $T$  from 0.002 to 0.02 in 0.002 steps. (c2)–(f2) Three-dimensional view of the reconstruction results obtained from ICS-DCT with different  $T$  from 0.002 to 0.02 in 0.002 steps. All images are normalized by the maximal values of the reconstruction results.

than those from Tikhonov. Although the ratio obtained from ICS-DCT is slightly higher than that from Tikhonov, the concentration difference between two fluorescent targets can still be reflected to some extent.

### C. Influence of Different Thresholds in DCT Filter

The influence of different thresholds ( $T$ ) in DCT filter is further analyzed in this section. According to the principle of DCT filter, the noise is mainly concentrated in the small values components of  $X_k^{\text{dct}}$ . If a relatively large  $T$  is set in 3-D DCT filter, some useful information may be removed from the reconstruction results. On the contrary, the noise information may not be suppressed effectively with a small  $T$ . Therefore, the reconstruction results and their quantitative analysis for different  $T$  from 0.002 to 0.02 in 0.002 steps are presented in this section.

In the phantom experiment with homogeneous background, the reconstruction results obtained from ICS-DCT with different  $T$  are shown in Fig. 8. As  $T$  increases, the reconstructed fluorescent targets first get closer to the true targets, and then, their volumes become larger than the true one. The REs of the slice results [see Fig. 8(c1)–(f1)] is presented in Fig. 9(a). The RE of the results obtained from ICS-DCT decreases dramatically when  $T$  increases from 0.002 to 0.006 and decreases very slowly when  $T$  increases from 0.006 to 0.014. The RE starts to slightly increase when  $T$  continues increasing. The RE of the results obtained from ICS without DCT filter is higher than those from ICS-DCT. As shown in Fig. 9(b), the CNRs of the 3-D results obtained from ICS-DCT with different  $T$  remain higher than that from ICS without DCT filter. And the CNR from

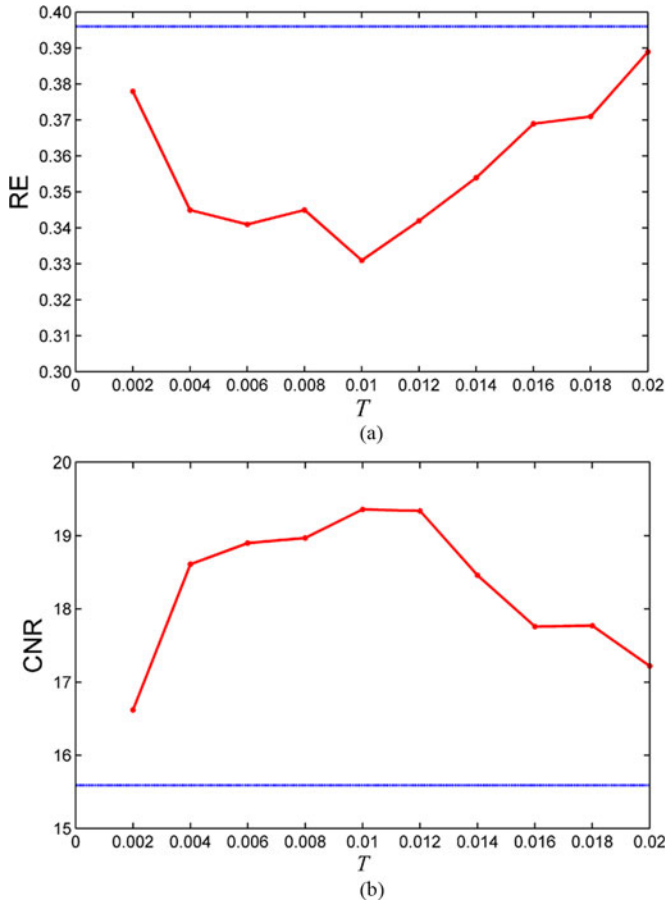


Fig. 13. Relative quantitation analysis of the reconstruction results in Fig. 12. (a) REs of the slice results obtained from different methods. (b) CNRs of the 3-D results obtained from different methods. The red line describes the REs and CNRs of the results obtained from ICS-DCT with different  $T$ . The blue line denotes the RE and CNR of the results obtained from ICS.

ICS-DCT first increases with  $T$  until it reaches its maximum value at  $T = 0.008$ , and then decreases with  $T$ .

In the phantom experiment with heterogeneous background and same strength of fluorescent targets, the reconstruction results obtained from ICS-DCT with different  $T$  are shown in Fig. 10. The reconstructed fluorescent targets get closer to the true targets as  $T$  increases. The REs of the slice results [see Fig. 10(c1)–(11)] are presented in Fig. 11(a). The REs of the results obtained from ICS-DCT are lower than that from ICS without DCT except when  $T \leq 0.004$ . As shown in Fig. 11(b), the CNRs of the 3-D results obtained from ICS-DCT with different  $T$  keep higher than the CNR of the results obtained from ICS without DCT filter. Besides, the CNRs of the results from ICS-DCT reach its maximum value at  $T = 0.01$ .

Fig. 12 shows the reconstruction results obtained from ICS-DCT with different  $T$  for the phantom experiment with heterogeneous background and different strengths of fluorescent targets. Similarly to the first two experiments, the REs of the results obtained from ICS-DCT decrease at first and then increase along the increase of the thresholds  $T$  [see Fig. 13(a)]. And the CNRs of the results from ICS-DCT increase first and then decrease with the increase of  $T$  [see Fig. 13(b)]. The REs

TABLE II  
2-NORM OF RESIDUAL  $\|WX - b\|_2$  AND MEASUREMENT VECTOR  $\|b\|_2$   
OBTAINED FROM THE PROPOSED ICS-DCT METHOD

2-Norm	Experiment 1	Experiment 2	Experiment 3
$\ b\ _2$	57.40	46.14	49.39
$\ WX - b\ _2$	42.49	25.87	23.45
Percentage	74.0%	56.1%	47.5%

and CNRs reach their minimum and maximum when  $T = 0.01$ , respectively.

The appropriate range of  $T$  in 3-D DCT filter can be obtained from the phantom experimental results. According to the qualitative results in Figs. 8, 10, and 12, the reconstruction quality can be improved effectively when  $T$  is set smaller than 0.02. More specifically, according to the relative quantitation results of REs and CNRs in Figs. 9, 11, and 13, the reconstruction results are with relatively high quality (i.e., small REs and high CNRs) when  $T$  is set between 0.006 and 0.014.

## V. DISCUSSION AND CONCLUSION

In this paper, an iterative correction scheme is proposed to reduce the negative effect of high-intensity background fluorescence in FMT reconstruction. The results in each iteration of the Tikhonov algorithm are first filtered by 3-D DCT. Then, the filtered results are corrected based on L1 regularization using the two-step IST algorithm. The effect of background fluorescence in FMT can be reduced effectively because of the filtering of the intermediate results and the detail preservation and noise suppression of L1 regularization.

The phantom experiments with high-intensity homogeneous and heterogeneous background fluorescence were conducted to demonstrate feasibility and advantage of the proposed method in this paper. Although the average values of different fluorescent targets obtained from the proposed method are higher or lower than those from the other methods in different experiments, as shown in Table I, the concentration ratios of different fluorescent targets can be reflected basically. Furthermore, the reconstruction quality of the results obtained from the proposed method is significantly improved in terms of the RE and CNR.

It is worth mentioning that the final residual of the proposed method is relatively large. As listed in Table II, the percentages of the 2-norm of the final residuals and that of the measurement vectors were 74.0%, 56.1%, and 47.5% in three experiments, respectively. Due to the aim of recovering only the fluorescent targets in this paper, the relatively poor fit is deemed acceptable.

An identity matrix is considered as the observation matrix  $H$  in (10) for simplicity. A weighted observation matrix determined by the intermediate result vector [15] may further improve the reconstruction quality and will be studied in the future.

## REFERENCES

- [1] V. Ntziachristos, "Fluorescence molecular imaging," *Annu. Rev. Biomed. Eng.*, vol. 8, no. 1, pp. 1–33, 2006.



- [2] M. Gao *et al.*, "Effects of background fluorescence in fluorescence molecular tomography," *Appl. Opt.*, vol. 44, no. 26, pp. 5468–5474, Sep. 10, 2005.
- [3] A. Soubret and V. Ntziachristos, "Fluorescence molecular tomography in the presence of background fluorescence," *Phys. Med. Biol.*, vol. 51, no. 16, pp. 3983–4001, Aug. 21, 2006.
- [4] A. Ale *et al.*, "Fluorescence background subtraction technique for hybrid fluorescence molecular tomography/x-ray computed tomography imaging of a mouse model of early stage lung cancer," *J. Biomed. Opt.*, vol. 18, no. 5, p. 056006, May 2013.
- [5] D. Wang *et al.*, "High-performance fluorescence molecular tomography through shape-based reconstruction using spherical harmonics parameterization," *Plos One*, vol. 9, no. 4, pp. 1–11, Apr. 14, 2014.
- [6] R. C. Haskell *et al.*, "Boundary conditions for the diffusion equation in radiative transfer," *J. Opt. Soc. Am. A*, vol. 11, no. 10, pp. 2727–2741, Oct. 11, 1994.
- [7] J. Ripoll *et al.*, "Fast analytical approximation for arbitrary geometries in diffuse optical tomography," *Opt. Lett.*, vol. 27, no. 7, pp. 527–529, Apr. 1, 2002.
- [8] M. Hanke and C. W. Groetsch, "Nonstationary iterated Tikhonov regularization," *J. Optim. Theor. Appl.*, vol. 98, no. 1, pp. 37–53, Jul. 1998.
- [9] J. Chamorro-Servent *et al.*, "Use of Split Bregman denoising for iterative reconstruction in fluorescence diffuse optical tomography," *J. Biomed. Opt.*, vol. 18, no. 7, p. 076016, Jul. 2013.
- [10] L. I. Bluestein, "A linear filtering approach to the computation of discrete fourier transform," *IEEE Trans. Audio Electroacoustics*, vol. AE-18, no. 4, pp. 451–455, Dec. 1970.
- [11] N. Ahmed *et al.*, "Discrete cosine transform," *IEEE Trans. Comput.*, vol. C-23, no. 1, pp. 90–93, Jan. 1974.
- [12] Y. Xu *et al.*, "Wavelet transform domain filters: a spatially selective noise filtration technique" *IEEE Trans. Image Process.*, vol. 3, no. 6, pp. 747–758, Nov. 1994.
- [13] R. Nowak and M. Figueiredo, "Fast wavelet-based image deconvolution using the EM algorithm," in *Proc. 35th Asilomar Conf. Signals, Syst., Comput.*, Nov. 2001, vol. 1, pp. 371–375.
- [14] M. Figueiredo *et al.*, "Majorization–minimization algorithms for wavelet-based image restoration," *IEEE Trans. Image Process.*, vol. 16, no. 12, pp. 2980–2991, Dec. 2007.
- [15] K. R. Rao *et al.*, "A new TwIST: Two-Step iterative shrinkage/thresholding algorithms for image restoration," *IEEE. Trans. Image Process.*, vol. 16, no. 12, pp. 2992–3004, Dec. 2007.
- [16] F. Liu *et al.*, "A parallel excitation based fluorescence molecular tomography system for whole-body simultaneous imaging of small animals," *Ann. Biomed. Eng.*, vol. 38, no. 11, pp. 3440–3448, Nov. 2010.
- [17] X. Cao *et al.*, "Accelerated image reconstruction in fluorescence molecular tomography using dimension reduction," *Biomed. Opt. Exp.*, vol. 4, no. 1, pp. 1–14, Jan. 1, 2013.
- [18] J. Shi *et al.*, "Efficient L1 regularization-based reconstruction for fluorescent molecular tomography using restarted nonlinear conjugate gradient," *Opt. Lett.*, vol. 38, no. 18, pp. 3696–3699, Sep. 15, 2013.

Authors' photographs and biographies not available at the time of publication.